

Spatially Resolved Elemental Analysis, Spectroscopy and Diffraction at the GSECARS Sector at the Advanced Photon Source

Stephen R. Sutton,* Antonio Lanzirotti, Matthew Newville, Mark L. Rivers, Peter Eng, and Liliana Lefticariu

Abstract

X-ray microprobes (XRM) coupled with high-brightness synchrotron X-ray facilities are powerful tools for environmental biogeochemistry research. One such instrument, the XRM at the Geo Soil Enviro Center for Advanced Radiation Sources Sector 13 at the Advanced Photon Source (APS; Argonne National Laboratory, Lemont, IL) was recently improved as part of a canted undulator geometry upgrade of the insertion device port, effectively doubling the available undulator beam time and extending the operating energy of the branch supporting the XRM down to the sulfur K edge (2.3 keV). Capabilities include rapid, high-resolution, elemental imaging including fluorescence microtomography, microscale X-ray absorption fine structure spectroscopy including sulfur K edge capability, and microscale X-ray diffraction. These capabilities are advantageous for (i) two-dimensional elemental mapping of relatively large samples at high resolution, with the dwell times typically limited only by the count times needed to obtain usable counting statistics for low concentration elements, (ii) three-dimensional imaging of internal elemental distributions in fragile hydrated specimens, such as biological tissues, avoiding the need for physical slicing, (iii) spatially resolved speciation determinations of contaminants in environmental materials, and (iv) identification of contaminant host phases. In this paper, we describe the XRM instrumentation, techniques, applications demonstrating these capabilities, and prospects for further improvements associated with the proposed upgrade of the APS.

Core Ideas

- X-ray microprobes are powerful tools for environmental biogeochemistry.
- Upgraded GSECARS XRM operates down to the sulfur K edge.
- Capabilities: spatially resolved elemental analysis, spectroscopy, and diffraction.
- Advanced Photon Source upgrade will further advance XRM capabilities.

HIGH-ENERGY synchrotron facilities produce X-radiation with high brightness, making them extremely powerful tools for a wide variety of spatially resolved research (Brown and Sturchio 2002; Sham and Rivers 2002; Sutton et al., 2002). The primary techniques, X-ray fluorescence (XRF) analysis, X-ray absorption fine structure (XAFS) spectroscopy, X-ray diffraction (XRD), and fluorescence microtomography (FCMT), are used to determine properties of heterogeneous materials, including chemical and phase compositions, crystallographic and other physical structures, and oxidation states (Sutton and Newville, 2014).

These X-ray microprobes (XRM) are common instruments at virtually every synchrotron facility (Sutton et al., 2006) and are typically heavily oversubscribed. Although there is general commonality in the analytical techniques, differences exist (primarily in the spatial resolution and energy range) that make available instruments highly complementary in their capabilities. Given that in environmental biogeochemistry research analyses at various spatial scales are required, the availability of a suite of instruments each optimized for analyses at different scales and targeting slightly different suites of elements benefits the broader community.

Focused X-ray beams can be produced using techniques that rely on collimation, refraction, diffraction, or reflection (Chu et al., 2008; Kang et al., 2008; Snigirev and Snigireva 2008). The most common focusing optics found in synchrotron X-ray probes are those based on diffraction or reflection. Full-field modes are also used where high spatial resolution is achieved via the detection components. Elemental imaging for focused beam X-ray probes is accomplished via raster scanning of samples through the beam. Improvements in detector electronics allow continuous, “fly-scanning” approaches to compositional imaging that provide greatly reduced mapping times.

Research using these X-ray probes has led to important insights into the geochemistry of toxic metals and metalloids in

S.R. Sutton and M.L. Rivers, Dep. of Geophysical Sciences, Univ. of Chicago, Chicago, IL 60637; S.R. Sutton, A. Lanzirotti, M. Newville, M.L. Rivers, and P. Eng, Center for Advanced Radiation Sources (CARS), Univ. of Chicago, Chicago, IL 60637; L. Lefticariu, Dep. of Geology and Environmental Resources and Policy Program, Southern Illinois Univ. at Carbondale, Carbondale, IL 62901. Assigned to Associate Editor Ganga Hettiarachchi.

Abbreviations: AMD, acid mine drainage; APS, Advanced Photon Source; CCD, charge-coupled device; DMRB, dissimilatory metal-reducing bacteria; EXAFS, extended X-ray absorption fine structure; FCMT, fluorescence microtomography; FWHM, full width at half maximum; GSECARS, Geo Soil Enviro Center for Advanced Radiation Sources; HPA, high-permeability area; KB, Kirkpatrick-Baez; LPA, low-permeability area; MBA, multibend achromat; nNP, neoformed nano- and microscale particles; SDD, silicon drift diode; SSA, secondary source aperture; XAFS, X-ray absorption fine structure; XANES, X-ray absorption near edge structure; XRD, X-ray diffraction; XRF, X-ray fluorescence; XRM, X-ray microprobe.

Copyright © American Society of Agronomy, Crop Science Society of America, and Soil Science Society of America. 5585 Guilford Rd., Madison, WI 53711 USA. All rights reserved.

J. Environ. Qual.

doi:10.2134/jeq2016.10.0401

Supplemental material is available online for this article.

Received 13 Oct. 2016.

Accepted 12 Jan. 2017.

*Corresponding author (sutton@cars.uchicago.edu).

contaminated sediments and tailings, the efficiencies of contaminant remediation strategies, and how bioaccumulation processes affect the distribution of trace toxic metal species and manufactured nanoparticles in soils and organisms, for example.

Here we describe some of the recent advances in these techniques and applications at the Geo Soil Enviro Center for Advanced Radiation Sources (GSECARS) Sector 13 at the Advanced Photon Source (APS; Argonne National Laboratory, Lemont, IL). In particular, the insertion device beamline at the sector was recently upgraded to a canted undulator geometry, effectively doubling the available undulator beam time and extending the operating energy of the branch supporting the X-ray probe instrument down to the sulfur (S) K edge (2.3 keV). In this report, we focus on the associated XRM upgrade and applications demonstrating the new capabilities. Finally, we discuss potential new capabilities anticipated with the upgrade of the APS to a multibend achromat (MBA) lattice currently in the planning stages.

Canted Undulator Upgrade

The canted undulator upgrade of Sector 13 (Supplemental Fig. S1) involved addition of a second undulator, replacement of the magnetic array in the existing undulator, division of an existing experimental enclosure into two independent enclosures, and addition and modification of beamline components. A summary of the capabilities of the Sector 13 experimental stations is given in Supplemental Table S1, including source, monochromator, energy range, flux, spot size, instruments, and techniques.

The two undulators have been installed in a canted geometry (1-mrad cant) to provide two independent undulator sources. An existing enclosure was partitioned into two enclosures by adding a dividing wall, door, and pass-through shielded beam pipe. X-rays are provided to this new enclosure (13ID-E) by installing the second undulator, two horizontal deflecting mirrors, a dedicated monochromator for the 13ID-E station, and two independent photon shutters serving each branch. The new configuration provides X-radiation from an upstream, medium-energy undulator (3.6-cm device, 2.3–28 keV) to the X-ray microprobe. The downstream undulator (3.0-cm device) supplies both doubly focused monochromatic X-radiation from 5.6 to 65 keV and white beam to a surface diffractometer, a laser-heated diamond anvil cell apparatus, and a multianvil press. These latter three instruments each receive an increase in beam time of ~33% and the microprobe now operates continuously, doubling the total beam time available on the undulator beamline.

The two undulators reside in the 5-m straight section in the accelerator. Supplemental Fig. S2 shows the calculated brilliance of the previous GSECARS 33-mm period Undulator A, the new 3.6-cm period undulator for the dedicated microprobe (ID-E) beamline, and the 3.0-cm period undulator for the surface scattering (ID-C) and high-pressure (ID-D) beamline. Note that the 3.6-cm period undulator extends to a lower energy than Undulator A (2.3 keV), and the 3.0-cm period undulator has twice the brilliance of Undulator A at the high energies used in the large-volume press. The two undulators combined produce a maximum of 8 kW of power at a ring current of 100 mA. The canted undulator front end is designed to handle up to 20 kW of power (providing a power buffer for future undulator and

ring current upgrades) and deliver the two independent photon beams to the experimental stations. The preexisting monochromator (which now serves the ID-C and ID-D branch exclusively) was modified to deliver either silicon (Si)(111), Si(311), or white beam radiation to the C and D stations (C or D can operate at any given time) while not interfering with the new canted beam that passes outboard of its crystal cage.

Dedicated X-Ray Microprobe (13ID-E) Beamline Configuration

The GSECARS microprobe (Fig. 1) uses microfocusing mirrors in a Kirkpatrick-Baez (KB) geometry to produce focused X-ray beams in the submicrometer size range. The beamline optics (Supplemental Fig. S3) provide submicrometer beams for the X-ray microprobe via a horizontal compound focusing geometry. In this configuration, the vertical focusing is obtained by an in-hutch, KB mirror, and the horizontal focusing is performed by combining two horizontal focusing mirrors. The first focusing mirror is the second mirror in the pair used to deflect the beam horizontally outboard; it operates at a pitch of 3 mrad and is capable of collecting 1.6 times the full width at half maximum (FWHM) of the horizontal undulator beam divergence. This long mirror creates a secondary source image at the location of a secondary source aperture (SSA), the adjustable opening of which provides a convenient way of controlling the horizontal source size seen by the second horizontal focusing mirror, located in the experimental station and one of the final KB mirror pair. The new 3.6-cm period undulator and monochromator installed as part of the canted upgrade allows us to produce focused monochromatic beam with energies down to the S K edge for the first time. The double-crystal monochromator is cryogenically cooled and sits upstream of the deflecting mirrors. The system incorporates both Si(111) and Si(311) crystals, which are translated into the beam as needed without interfering with either the monochromatic or white beam radiation transported to the ID-C and ID-D branch of the sector. The monochromator has fixed offset, bounces the beam up by 25 mm, and uses a state-of-the-art, air-bearing turntable with a ferrofluid vacuum seal for highly stable rotations, along with on-axis encoder systems using the latest products and technologies to give extremely accurate and reproducible energies over the full

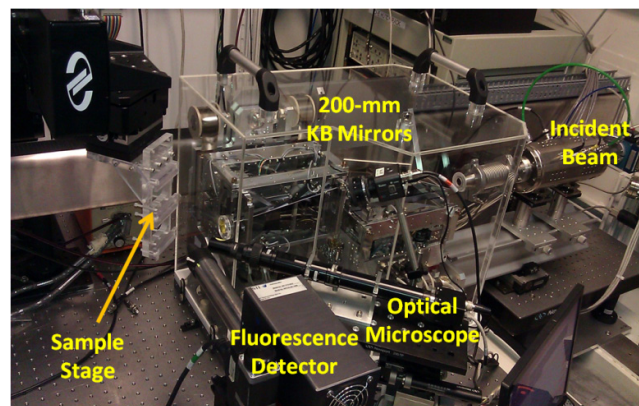


Fig. 1. View of the typical 13ID-E X-ray microprobe configuration including 240-mm-long vertical and horizontal Kirkpatrick-Baez (KB) mirrors, sample stage, optical microscope, and Vortex ME4 fluorescence detector.

energy range required for the beamline (for more information, see IDT, 2011). The monochromator has no significant energy drift (<0.05 eV) and continuous monitoring of energy calibration is typically unnecessary.

The microprobe operates in a “45°” geometry with the sample plane 45° to the microfocussed incident beam, an optical video microscope along the sample surface normal, a fluorescence detector at 90° to the incident beam (within the horizontal plane of the synchrotron for polarization reasons), and either an area detector for XRD studies or an ion chamber downstream of the sample for measuring X-ray sample absorption.

Microfocusing System

The upgraded microfocusing KB system (IDT, Supplemental Fig. S3) consists of two, 240-mm-long, highly polished Si mirrors, each with two distinct surfaces consisting of stripes of either bare Si or rhodium (Rh). Translators running perpendicular to the beam direction allow X-ray reflections to occur on one of the desired surfaces, the optimum one depending on the desired high-energy cutoff for specific experiments. Bare Si is valuable for low-energy operations and produces the lowest energy reflection cutoff for harmonic rejection. The Rh surface is useful for high-energy operations because it reflects X-rays to moderately high energy (lowest angle), up to the highest incident beam energy generally used at ID-E (typically 28 keV, cadmium [Cd] K edge spectroscopy). In conjunction with an SSA, the system is designed to generate focused beam spots with FWHM ranging from 7- μm height \times 0.5- μm volume with the SSA open, down to 1.7- μm height \times 0.5- μm volume with the SSA closed to a horizontal opening of 50 μm , effectively trading spatial resolution for flux. Horizontal sizes below 1 μm can be achievable by reducing the SSA size further.

Sample Stage

The sample stage is an x - y - z - θ configuration of positioning stages (Newport Corporation) with submicrometer repeatability and 20-cm horizontal and vertical travel range. On top of this “coarse” macrostage sits a high-resolution x - y stage with sub-100-nm repeatability, 25-mm travel in the horizontal direction, and 5-mm travel in the vertical direction. The high-resolution stages are used primarily for high-resolution mapping with the stages run in slew mode. The optical sample-viewing system uses an optical tube, typically with a 10 \times Mitutoyo, infinity-corrected, long working distance objective and a Point-Gray visible-light charge-coupled device (CCD). This arrangement produces a field of view of ~ 500 μm . In addition, a beam splitter can be incorporated in the optical path to allow for ultraviolet excitation using a Navitar ultraviolet imaging illuminator. This allows for general epifluorescence microscopy of specimens (particularly biological tissue) that have been intentionally exposed to ultraviolet-fluorescent stains.

X-Ray Fluorescence Detectors

The XRF detectors are Si drift diode (SDD) arrays, particularly the Vortex ME4 (Hitachi), which houses four independent 50-mm² detectors in a single snout. The advantages of these detectors are (i) that they are cooled by a thermoelectric cooler (no need for liquid nitrogen cooling), (ii) that they retain excellent energy resolution

within a broad range of peaking times (<136 eV FWHM at manganese [Mn] K α is typical), and (iii) that they provide high count rate (input rate >2.5 million counts s^{-1}). For example, at a very short peaking time of 0.25 μs , the ME4 detector can achieve a sustained output count rate of >3 million counts s^{-1} . A limitation of most commercially available SDD detectors is that the Si crystals are relatively thin (~ 300 μm), so they begin to become transparent as X-ray energy exceeds ~ 15 keV, thus losing efficiency. The pulse-processing electronics are provided by an Xpress 3 digital X-ray processor system (Quantum Detectors). The Xpress 3 system maximizes output count rate through automated adaptive filtering, rather than the more conventional use of fixed shaping or peaking times. This optimizes the output for each sample for mapping and spectroscopy applications without user intervention. A high-energy-resolution wavelength spectrometer (Oxford Instruments WDX-600, formerly Microspec) is also available for situations where resolutions in the ~ 10 -eV range are required to deconvolute peak overlaps. This instrument uses a Johansson geometry based on a mechanism to maintain the X-ray counter on the Rowland circle for point-to-point detection. Two proportional counters are mounted in tandem, one flowing P-10 gas and one sealed with 0.2-MPa xenon, the latter for absorption of high-energy X-rays. Slits define the angular acceptance and energy resolution. A six-crystal turret includes analyzing crystals such as LiF(200), LiF(220), LiF(420), and PET. Ion chambers are typically used both upstream and downstream of the sample for incident beam normalization, as well as collection of extended XAFS (EXAFS) spectra in transmission mode.

X-Ray Diffraction Detectors

Area detectors can be placed downstream of the sample to collect diffraction patterns in transmission mode. The most used XRD detector has been the PerkinElmer XRD1621 digital flat panel detector placed in transmission geometry ~ 400 mm downstream of the sample. The XRD1621 detector uses a 41-cm \times 41-cm amorphous Si sensor with a 2048-cm \times 2048-cm sensor size. The XRD1621 provides 200- μm pixel resolutions at 1 \times 1 binning, frame rates of 15 frames s^{-1} at 1 \times 1 binning and 30 frames s^{-1} at 2 \times 2 binning. This detector opens up the feasibility to perform near real-time μXRD for diffraction imaging and diffraction tomography. Area detectors that use CCD, such as the Rayonix 165, are also used for microdiffraction. The Rayonix 165 CCD can access a 2θ range from 1 to 35° (200-mm working distance) with 7 mdeg angular resolution and a relatively fast readout time of ~ 2 s. The MAR 345 image plate is larger, able to access up to 56° at about the same angular resolution, but has a much longer readout time of ~ 100 s.

Sample Environments

Various sample environments are available. Sample cooling can be achieved using either a Peltier-cooled sample stage or a continuous flow liquid helium cryostat. The former is appropriate for maintaining frozen water-bearing samples, such as ice cores. That latter can be advantageous when attempting to minimize photochemical effects caused by exposure to the intense X-ray beams. A Linkam 1500 heating stage can be used to maintain samples at nearly 1000°C during analysis. The new low-energy capabilities require a low-absorption environment, which is currently achieved using a helium-filled enclosure encompassing the incident beam and fluorescence beam paths, as well as the optical microscope path.

Analytical Techniques

The XRM is optimized for spatially resolved chemical analyses by XRF, speciation determinations using XAFS spectroscopy, phase identification using XRD, and applying all three of these methods in tomographic mode for three-dimensional insights with trace element sensitivity and submicrometer spatial resolution. The XRM is particularly powerful in studying the chemical nature of highly heterogeneous materials. These capabilities lead to unique opportunities in environmental biogeochemistry research. Here, we describe some of these analytical methods, as well as some example environmental biogeochemistry applications to highlight the recent advances.

Rapid, High-Resolution, Elemental Imaging of Large Specimens

The XRM is frequently used for producing two-dimensional elemental maps of samples with micrometer resolutions. Traditionally, these applications have used sample “stepping” methods, in which the sample stage is stepped to each map location, an XRF measurement accumulated for a set amount of time, the detector readout, and then to the next location. Such approaches were necessitated by the non-negligible amplifier and spectrometer readout times and, coupled with the stepping overhead, limited mapping speed. Due to developments in digital signal-processing electronics, most instruments have now adopted a slewing data collection approach, in which the sample stage is in continuous motion and measurements are obtained at regular intervals along the traverse. In this way, relatively large samples can be mapped at high resolution, with the dwell times typically limited by the count times needed to obtain usable counting statistics for low-concentration elements.

Typical elemental maps are built with a continuous scan for each row, rastering back and forth, with a small step between rows and time bins ranging from 5 to 100 ms. With 10-ms bins, a megapixel map covering 1×1 mm with $1\text{-}\mu\text{m}$ resolution takes about 3 h. Full XRF spectra are collected for each pixel and can be combined and analyzed in postprocessing software. Images extracted from predefined regions of interest in the XRF spectra for selected X-ray lines can be viewed and manipulated as the data are being collected.

An example of the XRF megapixel imaging is shown in Fig. 2. The image displays a three-color XRF compositional map showing the spatial distribution of calcium (Ca), zinc (Zn), and lead (Pb) in a thin section of *Lumbricus terrestris* Linnaeus, the common earthworm. The organisms had been exposed in vivo to soils contaminated with militarily relevant metals including tungsten and Pb. In this study (Seiter et al., 2012), the emphasis is on understanding the biogenic formation of metal-rich granules in earthworms from Pb-enriched soils. Studies show that earthworms will form mineral based granules with high concentrations of Pb and other metals found in the soils, thus rendering them nontoxic in their tissues and potentially limiting Pb mobility in natural settings (Seiter et al., 2012). This 1.2-megapixel image (1176×1031 pixels) of an earthworm posterior section images an area of 2.35×2.06 mm with $2\text{-}\mu\text{m}$ pixel size at 10 ms pixel^{-1} and took 3.3 h to collect.

Another example involves acid mine drainage (AMD) treatment. Pollutants in AMD are usually sequestered in neoformed nano- and microscale particles (nNP) through precipitation,

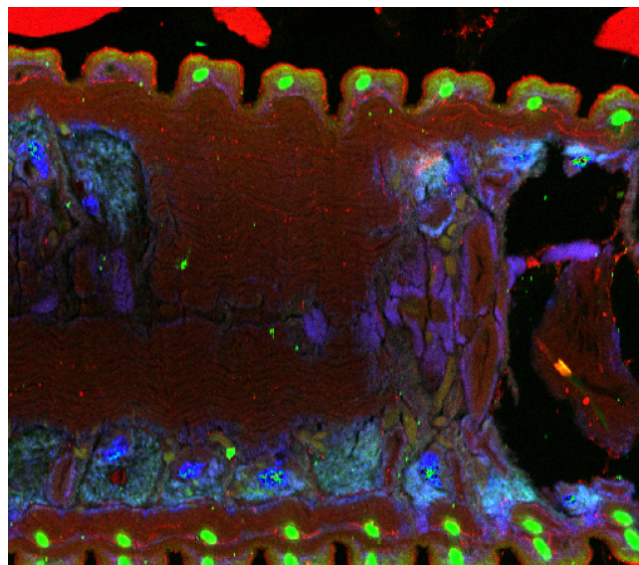


Fig. 2. X-ray fluorescence compositional map of the posterior section of an earthworm introduced to Pb-contaminated soil. Shown are fluorescence intensities for Ca $K\alpha$ (red), Zn $K\alpha$ (green) and Pb $L\alpha_1$ (blue). The image covers an area 2.35×2.06 mm in size and consists of 1.2 megapixels. Pixel size is $2\text{ }\mu\text{m}$ with 10 ms accumulation time per pixel. The Pb-rich areas in the earthworm digestive system shown in blue are where Pb has accumulated in biogenically formed metal-rich granules. The Zn-enriched areas at the earthworm margins in green are Zn localized in setae, growths on earthworm segments used for locomotion.

coprecipitation, and sorption. Subsequent biogeochemical processes may control nNP stability and thus long-term contaminant immobilization. Mineralogical, chemical, and microbiological data collected from sediments accumulated over a 6-yr period in a coal-mine AMD treatment system were used to identify the pathways of contaminant dynamics (Lefticariu et al., 2017).

Fast XRF elemental maps allowed large areas of AMD sediments to be studied and provided insight into the complex spatial distribution of key chemical elements (Fig. 3). Iron (Fe) was used as an nNP proxy because the nNP components are expected to be Fe-rich phases such as schwertmannite, goethite, lepidocrocite, and/or jarosite. The XRF maps showed contrasting spatial distribution of Fe in the samples from high-permeability areas (HPA) and low-permeability areas (LPA), being present as alternating bands of high and low Fe in the former and randomly distributed, small-scale, high-Fe spots in the latter. Gallium (Ga) served as a proxy for aluminum and clay-dNP (detrital nano- and micro-scale particles) since Ga^{3+} is incorporated into nonexchangeable framework positions in the phyllosilicate sheets (Brandt and Kydd, 1998). The Ga maps show an inverse correlation between Fe and Ga in HPA and a rather uniform distribution in LPA, suggesting ubiquitous presence of kaolinite. The presence of zirconium (Zr) hotspots (zircon grains) supports the existence of a significant detrital component in the AMD sediments.

Together with the other data from this study, the XRF maps provide evidence that clay minerals originating from the weathering of coal-mine waste facilitated the biogeochemical processes and ultimately the immobilization (facilitating heterogeneous nucleation and growth of nNP in oxic zones) and remobilization (promoting phase transformation and reductive dissolution of nNP in anoxic zones) of contaminants in the AMD sediments. A better understanding of these processes will likely lead to more effective treatment of pollutants at coal-mine-affected sites.

Fluorescence microtomography is essentially a two-dimensional XRF mapping method using a focused X-ray beam where one axis is rotation rather than translation. In this way, a so-called “sinogram” is produced, since a plot of fluorescence intensity on a translation versus rotation diagram produces a sine wave for each voxel in the object. In addition, since an energy-dispersive detector is used, sinograms for multiple elements are obtained simultaneously. An important limitation is that self-absorption of the fluorescence X-rays of interest cannot be too large. Such techniques readily produce two-dimensional maps of internal elemental distributions, and three-dimensional volumes can be obtained by translation of the object along the rotation axis and repeating. The fast mapping capability makes it more practical to collect such complete three-dimensional volumes. A major advantage in biogeochemistry is the ability to perform such internal imaging on hydrated specimens, such as biological tissues, avoiding the need for physical slicing.

The nondestructive nature of XRM makes the technique ideal for researchers examining genetic controls on metal

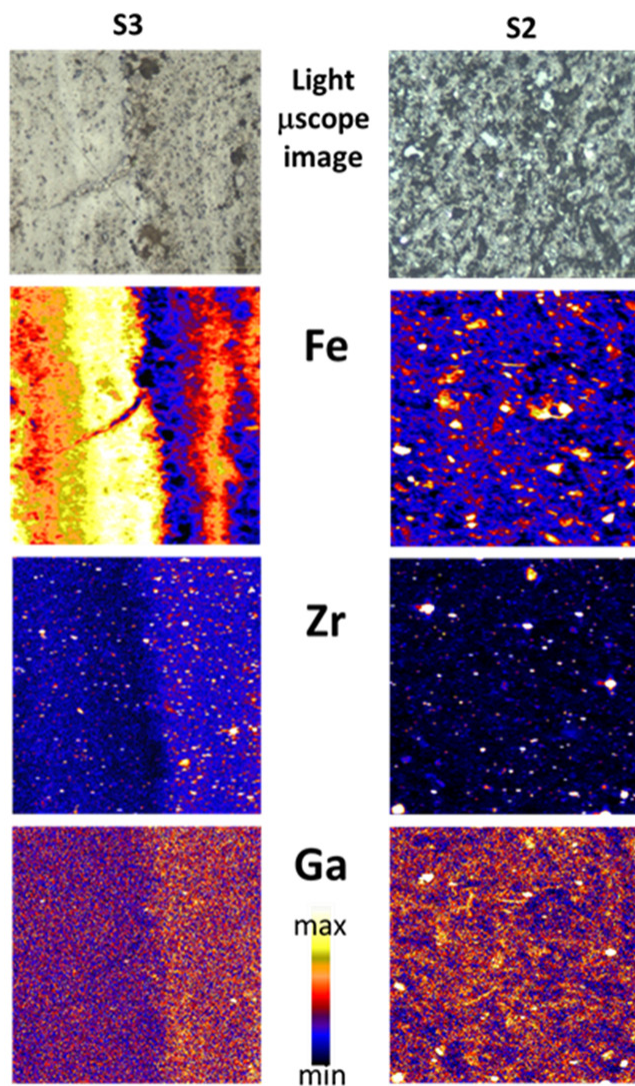


Fig. 3. Images of the acid mine drainage sediment samples: low permeability (LPA-S2, right) and high permeability (HPA-S3, left). Top images are visible light microscope images of the areas chosen for elemental mapping with the X-ray microprobe. Below those are the X-ray fluorescence maps for Fe, Zr, and Ga. All images are $500 \times 500 \mu\text{m}$, after Lefticariu et al. (2017).

homeostasis in plants. With FCMT, high-resolution three-dimensional imaging of the elemental composition of plants at a cellular level becomes feasible without the need for sample sectioning and fixation, which may alter elemental distributions. From a biogeochemical perspective, such studies provide important insight regarding how metals are mobilized from the rhizosphere to plants across cellular membranes (Punshon et al., 2009). Combining the use of FCMT with established genomic techniques, plant scientists are able to characterize the function of specific genes that control metal uptake. For example, Mn, an essential trace element, is important for plant health. Manganese deficiency can significantly limit crop yields and is a significant problem for crops grown in alkaline soils. Approximately one third of the world’s soils are considered too alkaline for optimal crop production. Socha and Guerinot (2014) have explored the use of FCMT to characterize the gene transporter families implicated in Mn transport in *Arabidopsis thaliana* (L.) Heynh., which may ultimately lead to new nutritionally enhanced crops that provide better agricultural yields in such nutrient-poor soils.

Figure 4 displays a single slice tomographic reconstruction of the distribution of Mn, Fe, and Zn in a seed of *A. thaliana*. Using high-speed electronics at 13-ID-E, this dataset was collected in continuous scan mode, with the rotation as the fast axis. The tomographic dataset is collected through 360° total rotation, with data collected every 0.3° of rotation every 15 ms. The reconstruction shown in Fig. 4 consists of 1210 angles and $400\text{-}\mu\text{m}$ horizontal translations ($1\text{-}\mu\text{m}$ increments), yielding a sinogram consisting of 480,000 pixels collected in ~ 1.5 h. Tomographic reconstruction using either filtered back-projection or algebraic iterative image reconstruction algorithms takes minutes at most for a single slice. However, advanced computational methods using penalized maximum-likelihood estimation have also been developed that allow for hyperspectral (spatio-spectral) image reconstruction of the XRF tomography signal (Gürsoy et al., 2015). With these advanced computation methods, it now becomes possible to tomographically reconstruct the full energy dispersive spectra without compromising the calculated XRF spectrum due to reconstruction artifacts.

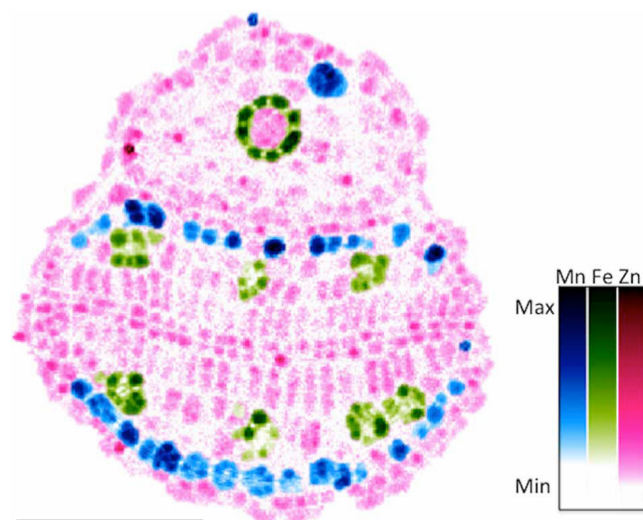


Fig. 4. Elemental distribution of Mn, Zn, and Fe in *A. thaliana* seeds collected using fluorescence microtomography. Shown is a two-dimensional map of a cross-section of an *A. thaliana* seed collected at $1\text{-}\mu\text{m}$ resolution; Mn (blue), Zn (magenta), and Fe (green) are shown, after Socha and Guerinot (2014).

Microscale XAFS Spectroscopy including Sulfur K Edge Capability

Micro-XAFS spectra are increasingly being used to quantify the valence states of multivalent elements (e.g., S, titanium [Ti], vanadium [V], chromium [Cr], Mn, Fe, europium, and uranium) in a wide variety of materials. Minerals and glasses have been studied extensively (Giuli et al., 2004; Sutton et al., 2005; Berry et al., 2008; Cottrell et al., 2009, and references therein; Karner et al., 2010).

The advantages of this approach include the element specificity, high spatial resolution, element sensitivity, and wide applicability range. Although the precise theory for the interpretation of X-ray absorption near edge structure (XANES) spectra remains under development, empirical approaches based on valence- and coordination-dependent shifts in intensity and energy of XANES features have been developed for extracting valence-state information. These empirical approaches tend to be element specific (i.e., the most valence-sensitive features can be different for different elements).

In biogeochemistry, valence determinations are useful in studies of reactive transport of contaminants, such as radionuclides in vadose zone sediments (Powell et al., 2006; Kaplan et al., 2007; Singer et al., 2009). Real-time XANES analyses of soil columns also can provide temporal information on speciation transformations during bioremediation processes (Tokunaga et al., 2008). In plant studies, XANES has become a useful technique for examining plant metal(loid) speciation (Donner et al., 2012; Sarret et al., 2013, and references therein), particularly in understanding contaminant toxicity and micronutrient availability and their metabolism in plant species.

The new 3.6-cm period undulator used by the XRM was chosen to allow access to lower energy absorption edges than previously accessible. Specifically, the new capabilities allow high-spatial-resolution XAFS spectra to be collected sequentially on absorption edges down to 2.3 keV (S K edge) and high-energy edges up to 28 keV (Cd K edge) on the same sample spot. Sulfur is a particularly important element with many different valences in nature (-2 to +6) and is a valuable probe for a wide variety of biogeochemical processes in sedimentary systems (Jones and Fike 2013).

The XRM allows XANES and EXAFS to be collected over the full energy range of the beamline by step scanning the energy, maintaining fixed offset, and coordinating the undulator gap to move to match the energy of the monochromator. In addition, the state-of-the-art monochromator allows "quick EXAFS" by continuously scanning the monochromator rotation axis and the separation between the two crystals to maintain fixed offset and to trigger the ionization and fluorescence detectors at fixed time intervals. Because the undulator gap also needs to be moved at high precision to match the energy of the monochromator, the fastest reliable per-energy time is 100 ms. Thus, continuous energy scanning allows a typical XANES or EXAFS scan of 500 energy points in about 1 min. Since the fluorescence detector has a fixed maximum count rate, a 1-min XANES scan is realistic only for fairly high-concentration ($>1000 \text{ mg kg}^{-1}$) elements or for standards measured in transmission mode.

Access to XRM instruments that can measure the S K absorption edge is particularly important for helping researchers understand the controls on biogeochemical cycling of nutrients and contaminants in subsurface environments. The redox cycling of S and Fe are often linked, so predicting the flow of electrons during

redox reactions involving these elements in the subsurface requires a fundamental understanding of the coupled biotic and abiotic processes responsible. Dissimilatory metal-reducing bacteria (DMRB) can use insoluble, extracellular substrates as electron acceptors for respiration and can reduce a variety of chemical compounds, such as ferric Fe. Flynn et al. (2014) undertook work involving SK μ XANES measurements at GSECARS and found that DMRB have the ability to transition from enzymatic reduction of Fe(III) minerals at circumneutral pH to a S⁰-reducing pathway at alkaline pH, providing a mechanism to sustain energy-generating electron transport processes over a much wider pH range than previously thought (Fig. 5). This pathway flexibility may be particularly relevant in expanding the conditions favorable for the retention of carbon (C) via siderite (FeCO₃) precipitation in the deep subsurface.

Another spectroscopy study focused on the mechanisms of mercury (Hg) removal by biochars (Liu et al., 2016). Micro-XRF mapping results indicate that Hg was heterogeneously distributed across biochar particles. Extended XAFS showed that Hg binding depended on the concentration of S, binding to S at high S content and to oxygen and chlorine at low S content. Sulfur XANES showed that both reduced and oxidized S species were present. Together, these data suggest that Hg removal is linked to the formation of chemical bonds between Hg and biochar functional groups. The presence of dissolved, Hg-complexing components is an important consideration when selecting biochars for different environmental applications.

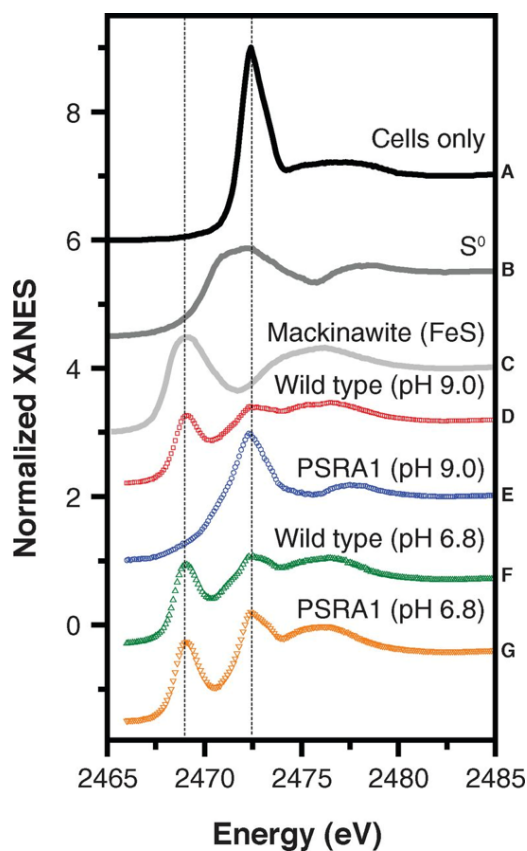


Fig. 5. Sulfur K micro-X-ray absorption near edge structure (XANES) spectra of standards and bioreactor products by Flynn et al. (2014). PSRA1 is a genetic mutant bacteria containing an in-frame deletion of the gene *psrA*. This study showed that some iron-reducing bacteria maintain a sulfur-reducing metabolic pathway, helping them to survive under alkaline conditions (see text).

Microscale X-Ray Diffraction

While XRM beamlines have incorporated detectors that allow for coupled μ XRF- μ XRD studies for many years (Lanzirotti et al., 2010), the slow readout time of the CCD area detectors that were generally used for diffraction analysis restricted most of this work to single-point analysis on a sample. The recent availability of high-speed digital flat panel detectors that are optimized for XRD provides new capabilities for high data throughput and real-time imaging of diffracted X-rays from a sample that can be coupled to the high-speed μ XRF imaging described above. For continuous μ XRD mapping, these detectors can collect data at rates faster than 30 frames s^{-1} while maintaining high resolution, good dynamic range, and contrast. This is a reasonably fast scan rate for megapixel imaging of XRD in a heterogenous material that is roughly comparable with scan rates employed in XRF mapping.

An example of a study that used this technique at the GSECARS XRM instrument is an extension of the AMD sediment study described above to include μ XRD measurements in an attempt to identify the host minerals of trace metals (Fig. 6). The 200×200 pixel ($400\text{-}\mu\text{m} \times 400\text{-}\mu\text{m}$) μ XRF compositional map was collected in continuous scanning mode with a $2\text{-}\mu\text{m}$ pixel size at a scan rate of 30 ms pixel^{-1} . Simultaneously with the XRF mapping, XRD area detector frames were collected for each pixel. Regions of interest were then defined on the map based on unique chemical features (e.g., areas of elevated copper [Cu]), and the XRD frames within this area were summed to provide an integrated XRD pattern. This takes advantage of the pixel averaging that summation provides to improve statistics and produce more powder-like patterns (Fig. 6). Such data can provide unequivocal mineralogical identification, particularly when coupled with elemental information, and allow for unique characterization of how chemical species are bound to specific mineral phases. Four Cu hotspots were selected, and XRD patterns were integrated over their areas (shown at right in Fig. 6). All four spots yield XRF spectra dominated by Fe with additional peaks from potassium, Ca, Ti, V, Cr, nickel, Cu, Zn, Ga, Pb, arsenic, rubidium, and strontium (Fig. 6). The XRD patterns were dominated by quartz, with clays also present. These data were interpreted to indicate that the trace elements are primarily incorporated in detrital clays that coat quartz grains.

The coupled application of μ XRF, XAFS, and XRD is a very attractive feature of the XRM at GSECARS. Karna et al. (2016) used this approach to understand the effect of organic C and S amendment on the promotion of stable host minerals for toxic elements (Pb, Zn, and Cd) in mine waste materials. The coupling of the synchrotron-based techniques was invaluable in enhancing the reliability of mineral identifications. They found that organic C amendment (with or without S amendment) facilitated sulfide formation, whereas carbonates dominated otherwise.

Some additional examples of the utilization of the application of coupled microfocused XRF, XAFS, and XRD mapping at the GSECARS XRM can be found in Lanzirotti et al. (2016), applied to studying contaminants associated with mine tailings and effluents.

Advanced Photon Source Upgrade

The APS is proposing a major upgrade to an MBA lattice. As a result, the brightness of the X-ray sources will be dramatically enhanced by reducing the electron beam emittance to the

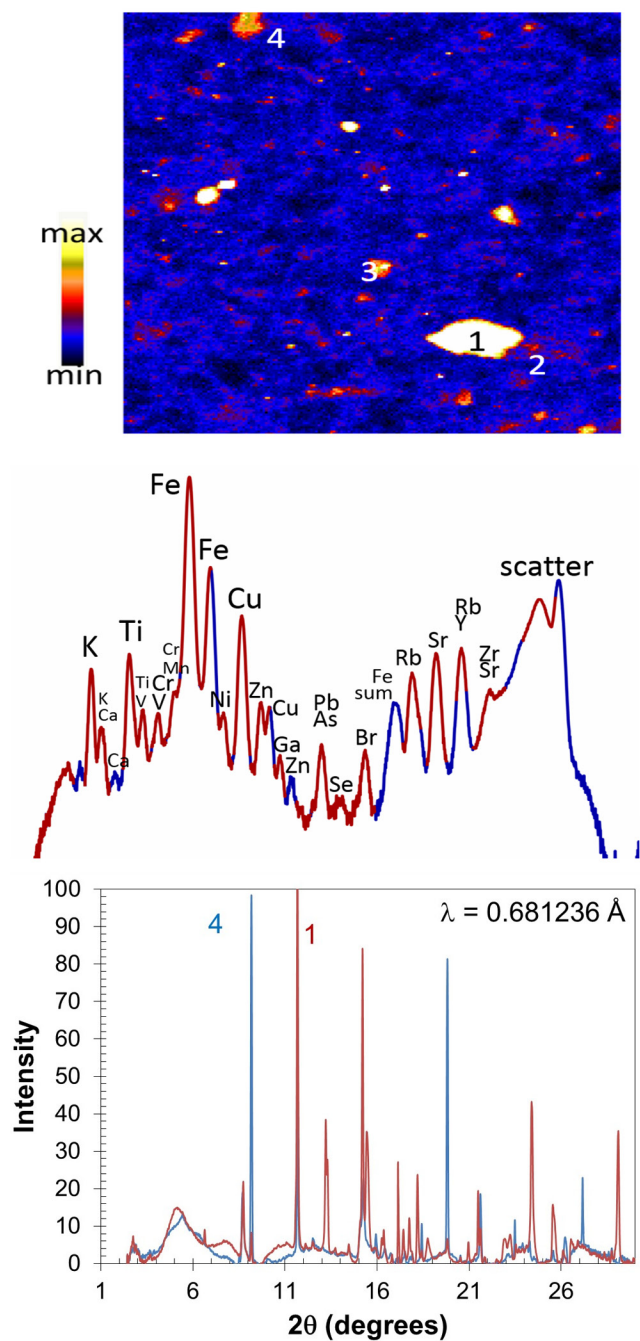


Fig. 6. Top: Copper map of acid mine drainage sediment sample S1. The image is $400 \times 400\ \mu\text{m}$ with $2\text{-}\mu\text{m}$ pixels and 30-ms dwell. The color bar shows the relationship between Cu concentration and color. Middle: The robust X-ray fluorescence spectrum for spot 1 in the top image, with Fe dominant and peaks also detected for K, Ca, Ti, V, Cr, Ni, Cu, Zn, Ga, Pb, As, Rb, and Sr. Bottom: X-ray diffraction patterns for spots 1 (red) and 4 (blue) showing diffraction peaks due to quartz and clays (predominantly kaolinite).

sub-100 pm-rad range, installing optimized small-gap undulators and increasing the ring current to 200 mA, among other improvements. In the current plan, the ring energy would be decreased from 7 to 6 GeV. X-ray brightness will be increased by two orders of magnitude (Supplemental Fig. S4). A white paper on the proposed MBA upgrade can be found in Borland (2014). A summary of early science at the upgraded APS can be found in APS (2015).

X-ray microprobe applications will be advanced through improved focusing capabilities, greater analytical sensitivity, and

enhanced analysis speed. In environmental biogeochemistry, the following XRM-based applications will benefit: (i) defining the trace element speciation at the nanoscales required to allow meaningful associations with nanostructural components within minute specimens such as oceanic biosilica structures, atmospheric aerosols, and organic components of soils, and (ii) interactions between microorganisms and minerals that control the speciation, migration, and toxicity of contaminated materials produced by natural processes and/or human activity.

Conclusions

X-ray microprobes are powerful tools for environmental biogeochemistry research. The XRM at the GSECARS Sector 13 at the APS was recently upgraded to effectively double the available undulator beam time, to extend the operating energy down to the S K edge, and to produce smaller, more intense, and stable beams. Rapid, high-resolution elemental imaging, μ XAFS, and μ XRD can be applied simultaneously and are advantageous for studying heterogeneous environmental biogeochemical materials. Some examples of applications in this field include determining the host phases of trace metals in AMD sediments, identifying genetic controls on metal homeostasis in plants, examining controls on biogeochemical cycling of contaminants in subsurface environments, and determining mechanisms of Hg removal by biochars. The capabilities of the XRM will be further improved with the advent of the proposed upgrade of the APS to an MBA lattice.

Acknowledgments

Portions of this work were performed at GSECARS (Sector 13), APS, Argonne National Laboratory. GSECARS is supported by the National Science Foundation–Earth Sciences (EAR-1128799) and Department of Energy–Geosciences (DE-FG02-94ER14466). Use of the APS was supported by the U S Department of Energy, Office of Science, Office of Basic Energy Sciences, under contract no. DE-AC02-06CH11357.

References

APS. 2015. Early science at the upgraded Advanced Photon Source. Advanced Photon Source, Argonne National Laboratory, Lemont, IL. <https://www1.aps.anl.gov/files/download/Aps-Upgrade/Beamlines/APS-U%20Early-Science-103015-FINAL.pdf> (accessed 2 Feb. 2017).

Berry, A.J., L.V. Danyushevsky, H.S. O'Neill, M. Newville, and S.R. Sutton. 2008. Oxidation state of iron in komatiitic melt inclusions indicates hot Archaean mantle. *Nature* 455:960–963. doi:10.1038/nature07377

Borland, M. 2014. Preliminary expected performance characteristics of an APS multi-bend achromat lattice. Advanced Photon Source, Argonne National Laboratory, Lemont, IL. <https://www1.aps.anl.gov/files/download/Aps-Upgrade/multi-bend-achromat-lattice.pdf> (accessed 2 Feb. 2017).

Brandt, K.B., and R.A. Kydd. 1998. Gallium and chromium substitution for aluminum in synthesized beidellite. *Clays Clay Miner.* 46:139–144. doi:10.1346/CCMN.1998.0460203

Brown, G.E., Jr., and N.C. Sturchio. 2002. An overview of synchrotron radiation applications to low temperature geochemistry and environmental science. *Rev. Mineral. Geochem.* 49:1–115. doi:10.2138/gsrmg.49.1.1

Chu, Y.S., J.M. Yi, F. De Carlo, Q. Shen, W.K. Lee, H.J. Wu et al. 2008. Hard-X-ray microscopy with Fresnel zone plates reaches 40 nm Rayleigh resolution. *Appl. Phys. Lett.* 92:103119. doi:10.1063/1.2857476

Cottrell, E., K. Kelley, A. Lanzirrotti, and R. Fischer. 2009. High-precision determination of iron oxidation state in silicate glasses using XANES. *Chem. Geol.* 268:167–179. doi:10.1016/j.chemgeo.2009.08.008

Donner, E., T. Punshon, M.L. Guerinot, and E. Lombi. 2012. Functional characterisation of metal(loid) processes in plants through the integration of synchrotron techniques and plant molecular biology. *Anal. Bioanal. Chem.* 402:3287–3298. doi:10.1007/s00216-011-5624-9

Flynn, T.M., E.J. O'Loughlin, B. Mishra, T.J. DiChristina, and K.M. Kemner. 2014. Sulfur-mediated electron shuttling during bacterial iron reduction. *Science* 344:1039–1042. doi:10.1126/science.1252066

Giuli, G., E. Paris, C. Romano, and D. Dingwell. 2004. V oxidation state and coordination number in silicate glasses by XAS. *Am. Mineral.* 89:1640–1646. doi:10.2138/am-2004-11-1208

Gürsoy, D., T. Biçer, A. Lanzirrotti, M.G. Newville, and F. De Carlo. 2015. Hyper-spectral image reconstruction for X-ray fluorescence tomography. *Opt. Express* 23:9014–9023. doi:10.1364/OE.23.009014

IDT. 2011. Air bearing DCM. Instrument Design Technology, Cheshire, UK. http://www.idtnet.co.uk/air_bearing_dcm.html (accessed 2 Feb. 2017).

Jones, D.S., and D.A. Fike. 2013. Dynamic sulfur and carbon cycling through the end-Ordovician extinction revealed by paired sulfate-pyrite $\delta^{34}\text{S}$. *Earth Planet. Sci. Lett.* 363:144–155. doi:10.1016/j.epsl.2012.12.015

Kang, H.C., H. Yan, R.P. Winarski, M.V. Holt, J. Maser, C. Liu et al. 2008. Focusing of hard X-rays to 16 nanometers with a multilayer Laue lens. *Appl. Phys. Lett.* 92:221114–221114. doi:10.1063/1.2912503

Kaplan, D., B. Powell, M. Duff, D. Demirkanli, M. Denham, R. Field, and F. Molz. 2007. Influence of sources on plutonium mobility and oxidation state transformations in vadose zone sediments. *Environ. Sci. Technol.* 41:7417–7423. doi:10.1021/es0706302

Karner, J.M., J.J. Papike, S.R. Sutton, P.V. Burger, C.K. Shearer, L. Le et al. 2010. Partitioning of Eu between augite and a highly spiked martian basalt composition as a function of oxygen fugacity (IW-1 to QFM): Determination of $\text{Eu}^{2+}/\text{Eu}^{3+}$ ratios by XANES. *Am. Mineral.* 95:410–413. doi:10.2138/am.2010.3394

Lanzirrotti, A., M. Newville, L. Manoukian, and K. Lange. 2016. High-speed, coupled micro-beam XRD/XRF/XAFS mapping at GSECARS: APS beamline 13-ID-E. In: T. Schäfer, R. Dohrmann, and H.C. Greenwell, editors, Filling the gaps: From microscopic pore structures to transport properties in shales. CMS workshop lecture series. Vol. 21. p. 53–64.

Lanzirrotti, A., R. Tappero, and D.G. Schulze. 2010. Practical application of synchrotron-based hard X-ray microprobes in soil sciences. *Dev. Soil Sci.* 34:27–72. doi:10.1016/S0166-2481(10)34002-5

Lefticariu, L., S.R. Sutton, K.S. Bender, M. Lefticariu, M. Pentrak, and J.W. Stucki. 2017. Impacts of detrital nano- and micro-scale particles (dNP) on contaminant dynamics in a coal mine AMD treatment system. *Sci. Total Environ.* 575:941–955. doi:10.1016/j.scitotenv.2016.09.154

Liu, P., C.J. Ptacek, D.W. Blowes, and R.C. Landis. 2016. Mechanisms of mercury removal by biochars produced from different feedstocks determined using X-ray absorption spectroscopy. *J. Hazard. Mater.* 308:233–242. doi:10.1016/j.jhazmat.2016.01.007

Powell, B.A., M.C. Duff, D.I. Kaplan, R.A. Fjeld, M. Newville, D.B. Hunter et al. 2006. Plutonium oxidation and subsequent reduction by Mn(IV) minerals in Yucca Mountain tuff. *Environ. Sci. Technol.* 40:3508–3514. doi:10.1021/es052353+

Punshon, T., M.L. Guerinot, and A. Lanzirrotti. 2009. Using synchrotron X-ray fluorescence microprobes in the study of metal homeostasis in plants. *Ann. Bot. (Lond.)* 103:665–672. doi:10.1093/aob/mcn264

Karna, R.R., G.M. Hettiarachchi, M. Newville, C. Sun, and Q. Ma. 2016. A synchrotron-based X-Ray spectroscopy studies for redox-based remediation of lead, zinc, and cadmium in mine waste materials. *J. Environ. Qual.* 45:1883–1893. doi:10.2134/jeq2015.12.0616

Sarret, G., E.A.H.P. Smits, H. Castillo Michel, M.P. Isaure, F.J. Zhao, and R. Tappero. 2013. Use of synchrotron-based techniques to elucidate metal uptake and metabolism in plants. *Adv. Agron.* 119:1–82. doi:10.1016/B978-0-12-407247-3.00001-9

Seiter, J., B. Lafferty, A. Bednar, S. Brasfield, A. Kennedy, and M. Chappell. 2012. Investigating bioavailability of militarily relevant metals using advanced molecular techniques. Annual meeting abstract. ASA, CSSA and SSSA, Madison, WI.

Sham, T.K., and M.L. Rivers. 2002. A brief overview of synchrotron radiation. In: P.A. Fenter, M.L. Rivers, N.C. Sturchio, and S.R. Sutton, editors, Applications of synchrotron radiation in low-temperature geochemistry and environmental sciences. Vol. 49. Mineralogical Society of America, Chantilly, VA. p. 117–147.

Singer, D.M., J.M. Zachara, and G.E. Brown, Jr. 2009. Uranium speciation as a function of depth in contaminated Hanford sediments—A micro-XRF, micro-XRD, and micro- and bulk-XAFS study. *Environ. Sci. Technol.* 43:630–636. doi:10.1021/es8021045

Snigirev, A., and I. Snigireva. 2008. High energy X-ray micro-optics. *C. R. Phys.* 9:507–516. doi:10.1016/j.cryh.2008.02.003

Socha, A.L., and M.L. Guerinot. 2014. Mn-coupling manganese: The role of transporter gene family members in manganese uptake and mobilization in plants. *Front. Plant Sci.* 5:1–16. doi:10.3389/fpls.2014.00106

Sutton, S.R., G.E. Brown, Jr., G. Calas, M.W. Caffee, M.T. Dove, R.J. Hemley, et al. 2006. User research facilities in the earth sciences. *Elements* 2(1):1–69. doi:10.2113/gselements.2.1.7

Sutton, S.R., P.M. Bertsch, M. Newville, M. Rivers, A. Lanzirrotti, and P. Eng. 2002. Microfluorescence and microtomography analyses of heterogeneous earth and environmental materials. *Rev. Mineral. Geochem.* 49:429–483. doi:10.2138/rmg.2002.49.8

Sutton, S.R., J.M. Karner, J.S. Delaney, J.J. Papike, C.K. Shearer, M. Newville et al. 2005. Vanadium K edge XANES of synthetic and natural basaltic glasses and application to microscale oxygen barometry. *Geochim. Cosmochim. Acta* 69:2333–2348. doi:10.1016/j.gca.2004.10.013

Sutton, S.R., and M. Newville. 2014. Synchrotron X-ray spectroscopic analysis. In: H.D. Holland and K.K. Turkianm, editors, Treatise on geochemistry. 2nd ed. Elsevier, Oxford, UK. p. 213–230. doi:10.1016/B978-0-08-095975-7.01415-7

Tokunaga, T., J. Wan, Y. Kim, S. Sutton, M. Newville, A. Lanzirrotti, and W. Rao. 2008. Real-time X-ray absorption spectroscopy of uranium, iron, and manganese in contaminated sediments during bioreduction. *Environ. Sci. Technol.* 42:2839–2844. doi:10.1021/es702364x